Engineering Geology 348 (2025) 107969

Contents lists available at ScienceDirect

Engineering Geology

journal homepage: www.elsevier.com/locate/enggeo

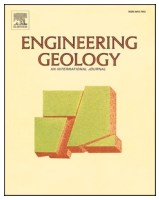

Pore-scale investigation of water-CO_2-oil flow in shale fractures for enhanced displacement efficiency and CO_2 sequestration

Xiangjie Qin [a], Han Wang [a], Yuxuan Xia [a], Xinghe Jiao [a], Gang Wang [b], Jianchao Cai [a,*]

[a] State Key Laboratory of Petroleum Resources and Engineering, China University of Petroleum, Beijing 102249, PR China
[b] College of Safety and Environmental Engineering, Shandong University of Science and Technology, Qingdao 266590, PR China

ARTICLE INFO

Keywords:
Water-CO_2-oil flow
CO_2 dissolution
Shale fracture network
Displacement efficiency

ABSTRACT

CO_2 geological sequestration plays an important role in energy and environmental sustainability. However, CO_2 channeling through fracture networks in shale reservoirs reduces sequestration efficiency. Injecting CO_2 followed by water flooding, driven by capillary forces, can suppress CO_2 channeling and enhance sequestration. This work establishes pore-scale models for CO_2-oil and water-CO_2-oil flows within three-dimensional shale fractures to explain this underlying mechanism. The volume of fluid method is employed to integrate the immiscible flow between water and a mixture fluid comprising CO_2 and oil, wherein the interaction between CO_2 and oil remains miscible and is governed by molecular convection-diffusion. The effects of contact angle, injection rate, and CO_2 volume on displacement are analyzed. The results show that high injection rates of CO_2 enhance the mass transfer between CO_2 and oil components, with the injection rate positively correlating with displacement efficiency. Water flooding following CO_2 injection suppresses CO_2 channeling attributable to capillary effects, resulting in an approximately 20 % enhancement in oil recovery compared to CO_2 flooding. Although a substantial volume of CO_2 reduces displacement pressure, it leads to a premature breakthrough. An increase in contact angle results in a large amount of mixture fluid being trapped in blind-end pores, corresponding to unsatisfactory displacement effects. Nonetheless, an increased water injection rate augments the contact between the water and the mixture fluid, facilitating CO_2 dissolution. This results in a gradual decline in outlet mass flow and enhancements in oil recovery and CO_2 sequestration efficiency.

1. Introduction

Carbon capture, utilization, and storage (CCUS) is an important strategy for reducing CO_2 emissions (Edwards and Celia, 2018; Davoodi et al., 2023). Meanwhile, CO_2 geological sequestration, as an effective carbon utilization and storage technology, has been widely applied to enhance the recovery of unconventional oil and gas resources (Wang et al., 2023b; Yang et al., 2023a). In unconventional reservoirs, CO_2 is typically in a supercritical state and is miscible with oil (Nguyen et al., 2018). Furthermore, the presence of formation water and injected water results in a multiphase multicomponent flow system involving water, CO_2, and oil (Song et al., 2024b). CO_2-rock-water interactions can take place in carbonate-rich rock formations, altering the reservoir pore structures (Khurshid and Afgan, 2021). As a result, the flow mechanisms include miscible and immiscible interactions within complex pore structures (Hao et al., 2022). Transport process is affected by microscopic mechanisms such as contact angle, interfacial tension, convection, and diffusion, which limits in-depth understanding of CO_2 enhanced oil recovery (EOR). Therefore, it is essential to develop a pore-scale model that incorporates these microscopic mechanisms to explain the complex displacement processes, thereby improving oil recovery and CO_2 sequestration efficiency.

Shale reservoirs contain numerous micro- and nanoscale pores, which are connected by microfractures created through fracturing techniques (Qin et al., 2024). Injected CO_2 invades the fractures and gradually diffuses into the matrix pores. Dissolved CO_2 reduces the density and viscosity of oil, enhancing mobility (Sambo et al., 2023). However, miscible CO_2 tends to flow through preferential pathways in fractures and heterogeneous pore structures, reducing sequestration efficiency (Wang et al., 2020). Injecting water into reservoirs can effectively suppress CO_2 channeling due to capillary effects, thereby enhancing sweep efficiency. Therefore, understanding the CO_2 dissolution characteristics and sweep efficiency in water-CO_2-oil displacement processes within fracture networks is crucial for developing effective

* Corresponding author.
E-mail address: caijc@cup.edu.cn (J. Cai).

https://doi.org/10.1016/j.enggeo.2025.107969
Received 14 September 2024; Received in revised form 12 February 2025; Accepted 12 February 2025
Available online 13 February 2025

production strategies.

Experimental and numerical methods are widely used to investigate CO_2-EOR in shale reservoirs (Massarweh and Abushaikha, 2022; Li et al., 2023). Core-flooding experiments obtain macroscopic displacement characteristics, and combined with nuclear magnetic resonance (NMR), the displacement efficiency in different pores can be quantitatively evaluated (Yu et al., 2022; Tang et al., 2023). However, experimental methods fail to describe the microscopic miscible flow mechanisms involving convection and diffusion. Additionally, it does not address the interface dynamics and non-wetting fluid trapping in immiscible flow processes. Although molecular dynamics (MD) simulations can explain the water-CO_2-oil flow mechanisms from molecular and atomic perspectives (Liu et al., 2022; Lu et al., 2023), their substantial computational requirements limit the modeling scale to single nanopores (Wang et al., 2022b). Pore-scale simulations have advantages in describing complex flow processes in porous media (Wang et al., 2022a; Zhou et al., 2023; Yang et al., 2024). On the one hand, geometry models reflecting the actual shale pore structures can be constructed based on micro/nano-computed tomography (CT) and focused ion beam scanning electron microscopy (FIB-SEM) experiments (Wang et al., 2021; Yu et al., 2024; Cai et al., 2025). On the other hand, developed pore-scale simulations can account for microscopic mechanisms such as convection, diffusion, and interface effects (Chen et al., 2022; Song et al., 2024a). This improves the modeling scale compared to MD simulations. Currently, extensive research has been conducted on CO_2-oil miscible flow based on pore-scale simulations. Chowdhury et al. (2022) investigated miscible CO_2 flooding under various reservoir conditions and injection rates. They found that sequestration efficiency is significant in light oil, with the injection rate positively correlated with oil recovery. Zhu et al. (2024) simulated miscible CO_2-oil flow in tight reservoirs, considering competitive adsorption, diffusion, and convection. They concluded that molecular diffusion and convection determine displacement patterns, while fracture distribution and connectivity significantly impact oil recovery. However, achieving satisfactory oil recovery may require injecting large volumes of CO_2 due to the absence of capillary effects in miscible CO_2 flooding. Behnoud et al. (2023) compared miscible and near-miscible CO_2 flooding processes. CO_2 preferentially displaces oil along large pore bodies under miscible conditions. In near-miscible conditions, CO_2 can invade smaller pore throats due to the capillary effect, increasing recovery from 92 % to 98 %. Therefore, CO_2 channeling in heterogeneous pore structures and fracture networks severely limits the recovery and sequestration effectiveness during miscible displacement.

CO_2 water-alternating-gas (WAG) injection can effectively reduce the rapid migration of CO_2 through preferential pathways (Afzali et al., 2022; Asemani and Rezaei, 2022). Injecting water during CO_2 miscible flooding enhances sweep efficiency and stability of the displacement front (Han et al., 2024). Additionally, the dissolved CO_2 is trapped in blind-end pores and complex pore networks (Fig. 1). However, the injected water leads to a complex multiphase multicomponent flow system of water-CO_2-oil within shale reservoirs. Only a few studies have explored complex multiphase multicomponent flow in shale reservoirs through pore-scale simulations. Wang et al. (2023a) considered CO_2-oil competitive adsorption and miscible flow, analyzing the impact of the water phase on shale oil recovery and CO_2 storage. Currently, research on the displacement process of water-CO_2-oil is insufficient, and the microscopic mechanisms by which water injection stabilizes the displacement process during CO_2 miscible flooding remain unclear. In addition, simulations are mostly carried out based on two-dimensional (2D) random porous media, which is significantly different from the actual three-dimensional (3D) pore-fracture structures. This results in various convection-diffusion interactions and capillary effects.

This work aims to establish a pore-scale model to explain the microscopic mechanisms by which the injected water phase inhibits CO_2 channeling and stabilizes the displacement process in actual 3D shale fracture networks. Firstly, a CO_2-oil miscible flow model is established, considering the convection and diffusion effects. Furthermore, a multiphase multicomponent model for water-CO_2-oil flow is integrated based on the volume of fluid (VOF) method. The mixture fluid composed of CO_2 and oil, governed by convection and diffusion, forms an immiscible flow system with water. Then, the CO_2-oil miscible and water-CO_2-oil displacement processes in the 3D fracture networks are simulated and compared. Finally, the effects of injection rates, CO_2 volume, and wettability on CO_2 dissolution and oil recovery are evaluated. This work provides insights into the flow characteristics of water-CO_2-oil within fracture networks from a microscopic perspective, helping to optimize the development strategies.

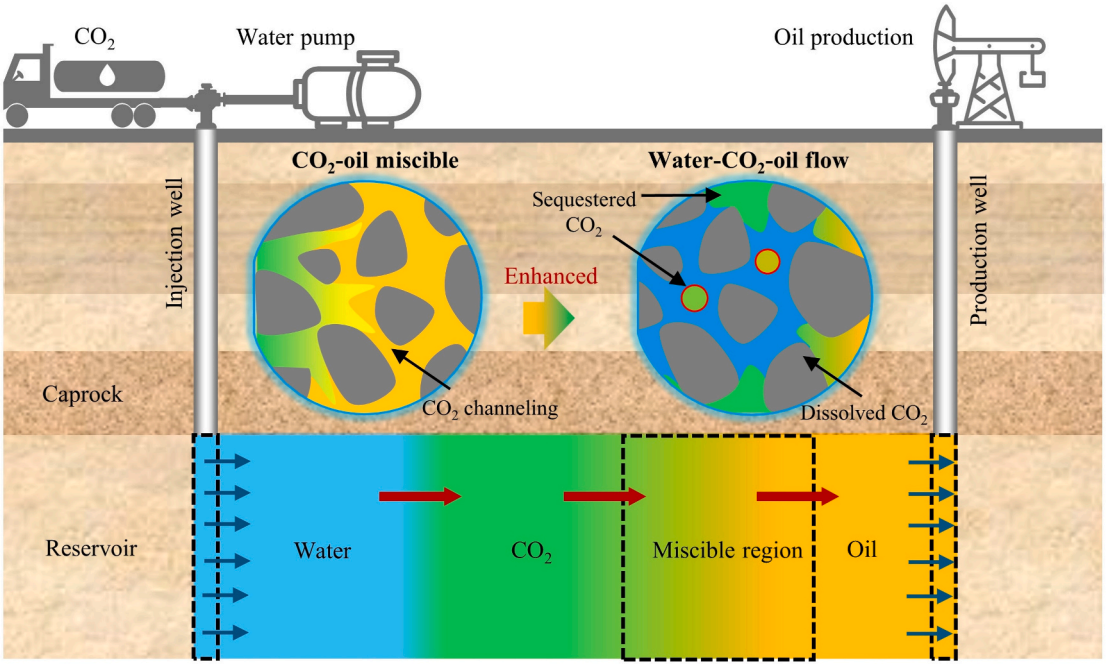

Fig. 1. Schematic diagram of CO_2 injection for enhanced oil recovery.

2. Geological setting

The Jiyang Depression, located in the southwest part of the Bohai Bay Basin, is shaped by multiple major deep faults, including the Chengnan and Chennan faults, forming a half-graben fault depression (Ma et al., 2023). The Jiyang Depression has been modified by multiple phases of tectonic activity, including Indosinian, Yanshanian, and Himalayan movements. The geological structure is complex, with a well-developed fault system, diverse sedimentary facies, and various types of oil reservoirs. The Niuzhuang subsag (Fig. 2), located within the Dongying sag in the southern part of the Jiyang Depression, is a fault-depression lake basin (Chen et al., 2017; Liu et al., 2023). The depression develops Kongdian, Shahejie, and Dongying Formation from bottom to top, with a sediment thickness of more than 3500 m. Dark muddy shale with a thickness of 800–1600 m developed in the lower Sha3 Member and upper Sha4 Member of the Shahejie Formation has great potential for the development of unconventional oil resources (Zhang et al., 2018). It is an important area for shale oil exploration and is also the research area of this work.

3. Reconstruction of 3D fracture structures

3.1. Formation of fractures

The shale sample from the NY1 well in the Niuzhuang subsag with a burial depth of more than 3000 m is selected for analysis. Fractured shale oil is abundant in this region, with a density of 0.85 g/cm^3 (Liu, 2022). Shale mineral composition affects fracture distribution characteristics, resulting in different fluid storage and transport properties. The clay mineral content is 34 %, and the quartz, calcite, and dolomite contents are 19 %, 22 %, and 10 % respectively (Table 1). The high content of brittle minerals is conducive to fracture formation (Zhao and Zhou, 2023). However, the presence of clay minerals increases the rock plasticity and leads to the complexity of fracture structures. The shale in the Jiyang Depression features extensively developed lamination structures. These lamination structures are superimposed with the natural fracture system of the continental fault basin, forming unique pore-fracture network systems with a strong flow capacity. Fracture structures enhance pore connectivity, allowing injected water and CO_2 to displace oil from the matrix pores during shale oil development. It is essential to investigate the sweep efficiency of CO_2 within fractures in water-oil-CO_2 systems for enhanced recovery.

Table 1
Mineral composition of the shale sample.

Minerals	Clay	Quartz	Calcite	Dolomite	Pyrite and siderite	Plagioclase
Contents (%)	34	19	22	10	11	3

3.2. Fracture identification based on micro-CT experiments

The cylindrical sample with a diameter of 1 mm is prepared using the wire cutting method. CT scanning is conducted at a resolution of 0.86 μm to capture detailed fracture structures, and 1000 2D grayscale slices are obtained with dimensions of 1000 × 1000 pixels. The images reveal that fracture structures develop in the shale sample and that only a small number of matrix pores are found due to resolution limitations (Fig. 3 (a)). In addition, scattered high-density minerals and banded clay minerals are distributed in the images. The 3D fracture structures are extracted through threshold segmentation, with a fracture aperture of approximately 3.5 μm. Due to the randomly distributed minerals, the fractures exhibit poor integrity (Fig. 3 (b)), forming a complex fracture network that results in complicated fluid flow mechanisms.

3.3. Fracture structure characterization

To quantitatively characterize fracture networks, the watershed algorithm combined with distance transformation is introduced to segment fracture systems (Qin et al., 2023), identifying throat structures and generating the corresponding fracture network (Fig. 3 (c)). Different fracture structures interconnected via the throats within the network, with an average connection degree of 3.5, which demonstrates strong connectivity. The distribution characteristics of the equivalent fracture and throat sizes are analyzed. Both fracture and throat sizes exhibit a unimodal distribution (Fig. 3 (d)). The equivalent fracture radii are predominantly within the range of 2 to 4 μm, accounting for 65.4 % of the total. Throat sizes are concentrated primarily between 1 and 2 μm, comprising 53.4 % of the total.

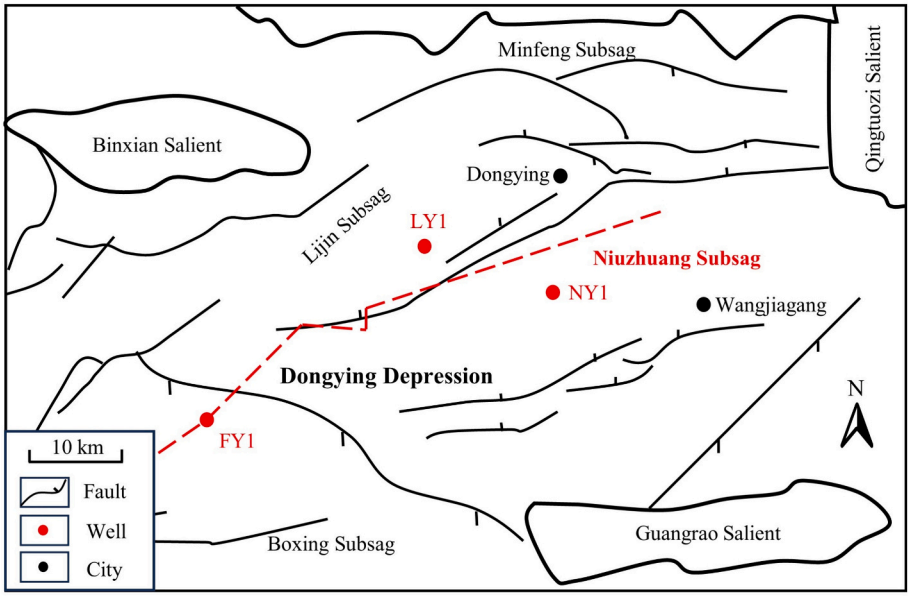

Fig. 2. Geographical location of the shale samples.

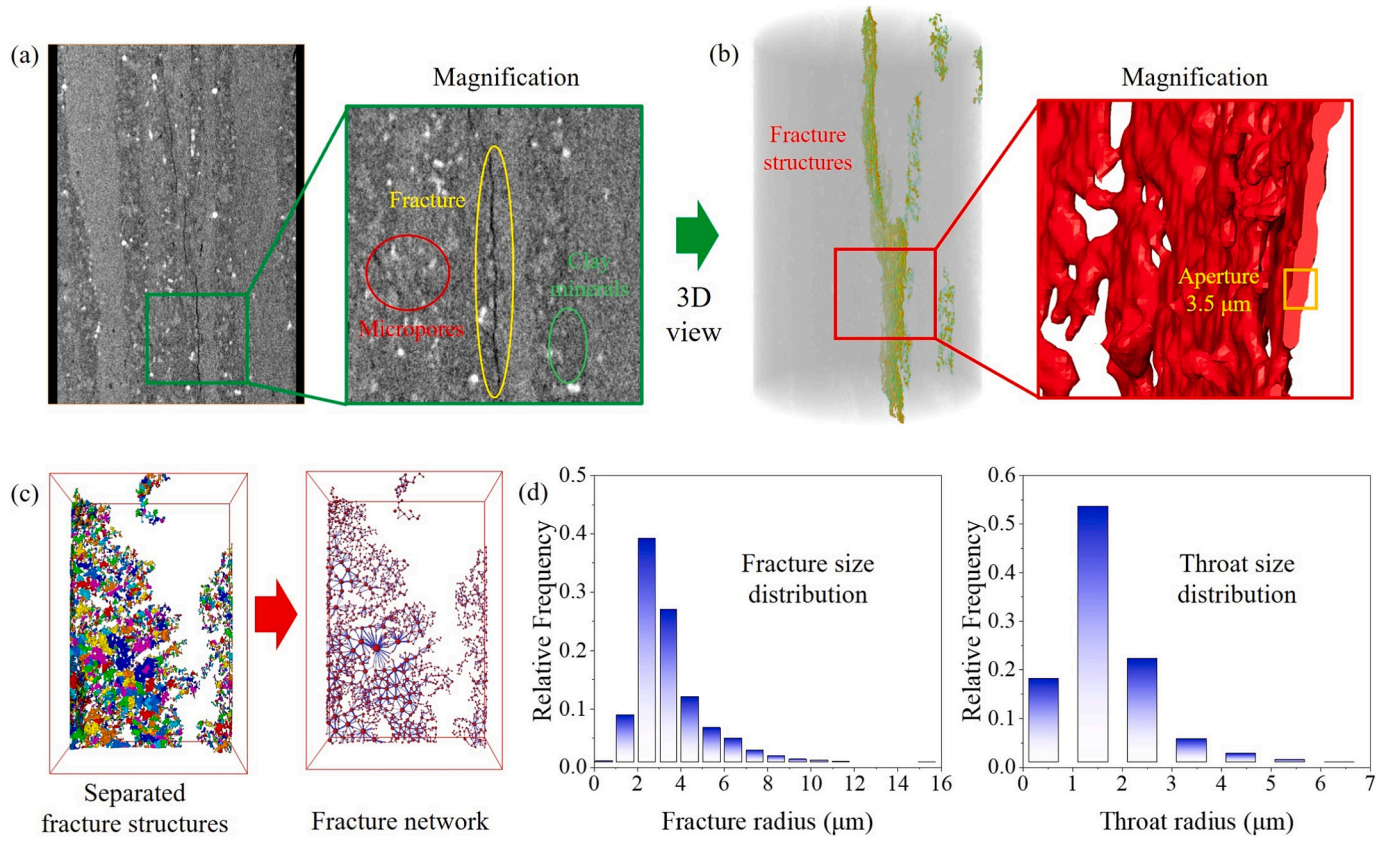

Fig. 3. Comprehensive characterization of shale fracture structures. (a) CT scanning results of the shale sample. (b) Reconstruction of the 3D fracture structure. (c) The fracture network generated based on the watershed algorithm. (d) Quantitative description of fracture structures.

4. Numerical model for water-CO_2-oil flow

A multiphase multicomponent flow numerical model is established for water-CO_2-oil flow in 3D shale fractures. The in-situ pressure of the shale reservoir is 65 MPa, and the temperature is 135 °C. Therefore, CO_2-oil is considered to exhibit miscible flows, while water-CO_2 and water-oil systems are assumed to involve immiscible flows with distinct interfaces. To achieve the multiphase multicomponent flow, a mixture fluid comprising CO_2 and oil components is defined, which forms an immiscible system with water (Fig. 4 (a)). The concentrations of CO_2 and oil in the mixture fluid are controlled by their respective mass fractions, while the mass transfer between CO_2 and oil is governed by convection and diffusion (Fig. 4 (b)).

4.1. CO_2-oil transport in mixture fluid

Various components of a fluid are mixed at the molecular scale in multicomponent flows and share the same mean velocity, pressure, and temperature fields. The mass transfer takes place by convection and diffusion. It is further assumed that the diffusion velocity of a component obeys Fick's law.

In multicomponent flow solutions, a single velocity field is computed for the fluid comprising multiple components. Individual components move at the velocity of the fluid of which they are part, with a drift velocity superimposed, arising from diffusion. The transport equation for bulk fluid flow is the Navier-Stokes equation. Nevertheless, additional equations are necessary to determine the transport mechanism of components within the fluid. The mass conservation equation for each component is (Punetha and Khandekar, 2017):

$$\frac{\partial \rho_i}{\partial t} + \frac{\partial (\rho_i \boldsymbol{u})}{\partial x} = -\frac{\partial m}{\partial x} \tag{1}$$

where ρ_i is the mass-average density of the fluid component i, $\boldsymbol{u}$ is the mass-averaged velocity field, and m is the relative mass flux term (diffusion-like term).

Sum all components in the expansion of Eq. (1) to obtain the

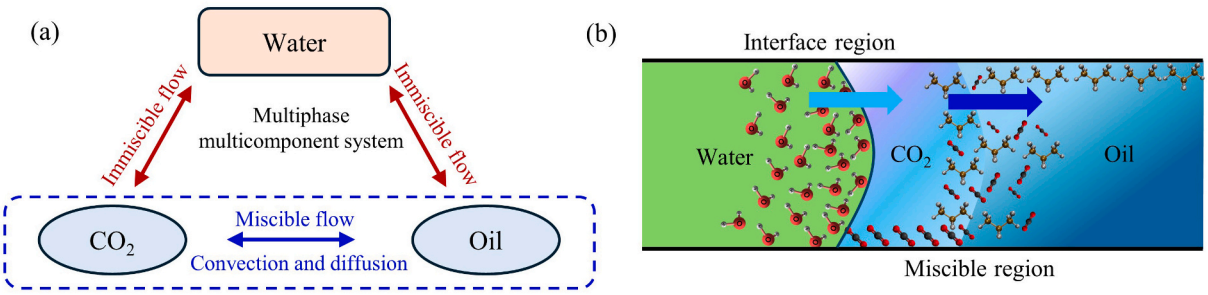

Fig. 4. Multiphase multicomponent water-CO_2-oil flow system. (a) Fluids composition and (b) flow mechanisms.

standard continuity equation (Shypul et al., 2022):

$$\frac{\partial \overline{\rho}}{\partial t}+\frac{\partial(\overline{\rho}\boldsymbol{u})}{\partial x}=0 \tag{2}$$

where $\overline{\rho}$ is the density of the mixture fluid.

The relative mass flux term accommodates the varying motion of individual components, which can be modeled to include effects such as concentration gradients, pressure differentials, external forces, and temperature gradients. Concentration primarily affects the relative motion between different components. The diffusion-like term in Eq. (1) considers this effect:

$$m=\rho_i(\boldsymbol{u}_i-\boldsymbol{u})=-\frac{\alpha}{\overline{\rho}}\frac{\partial \rho_i}{\partial x} \tag{3}$$

where α is the molecular diffusion coefficient, $\boldsymbol{u}_i$ is the mass-averaged velocity of the fluid component i.

The mass fraction φ_i of component i is defined as:

$$\varphi_i=\frac{\rho_i}{\overline{\rho}} \tag{4}$$

Substituting Eq. (3) and Eq. (4) in Eq. (1) gives the following:

$$\frac{\partial(\overline{\rho}\varphi_i)}{\partial t}+\frac{\partial(\overline{\rho}\boldsymbol{u}\varphi_i)}{\partial x}=\frac{\partial}{\partial x}\left(\alpha_i\frac{\partial \varphi_i}{\partial x}\right) \tag{5}$$

This is a general advection-diffusion equation of the form common to the equations solved for each of the dependent variables in the fluid flow calculation. Consequently, it is convenient to solve for the mass fraction to establish the composition of the mixture fluid. The sum of the mass fractions of all components invariably equals 1. This is enforced by specifying one component as the constrained component. The mass fraction of this component is always the difference between 1 and the sum of the mass fractions of all other components.

4.2. Calculation of fluid properties

The mixture fluid contains components of CO_2 and oil, and its properties are calculated from those of the constituent components. The calculated properties are employed to predict the global flow characteristics of the mixture fluid, while the transport between CO_2 and oil components within the mixture fluid is further affected by convection-diffusion. Fluid properties such as density and viscosity in multicomponent systems are closely related to the mass fraction. The partial volume (V_i) of component i calculated by the thermodynamic density (ρ_{si}) is defined. The sum of the partial volumes of all components must be the total volume V of the mixture fluid:

$$1=\sum_{i=A,B\ldots}^{N}\frac{V_i}{V}=\sum_{i=A,B\ldots}^{N}\frac{M_i/\rho_{si}}{M_i/\rho_i}=\sum_{i=A,B\ldots}^{N}\frac{\rho_i}{\rho_{si}}=\sum_{i=A,B\ldots}^{N}\frac{\overline{\rho}\varphi_i}{\rho_{si}} \tag{6}$$

where M_i is the mass of component i.

Therefore, the mixture density can be obtained by the mass fraction and the thermodynamic density of each component:

$$\frac{1}{\overline{\rho}}=\sum_{i=A,B\ldots}^{N}\frac{\varphi_i}{\rho_{si}} \tag{7}$$

In addition, arbitrary constitutive fluid properties such as viscosity can be obtained by:

$$\overline{\chi}=\sum_{i=A,B\ldots}^{N}\varphi_i\chi_i \tag{8}$$

where $\overline{\chi}$ and χ_i is the mixture fluid property and fluid property of fluid component i.

4.3. Multiphase multicomponent water-CO_2-oil flow

The immiscible multiphase flow and miscible multicomponent flow are combined to complete the water-CO_2-oil flow system. Specifically, a mixture fluid of CO_2 and oil constitutes a multicomponent flow system driven by advection-diffusion. The water and the mixture fluid form an immiscible multiphase flow system with a distinct interface. The VOF method is employed to solve immiscible multiphase flow processes (Yang et al., 2023b). By solving the momentum equation, all fluids share a common flow field in an immiscible multiphase flow system:

$$\frac{\partial(\rho\boldsymbol{u})}{\partial t}+\nabla\cdot\left(\rho\boldsymbol{u}\cdot\boldsymbol{u}-\mu\left(\nabla\boldsymbol{u}+(\nabla\boldsymbol{u})^T\right)\right)=F_s-\nabla p \tag{9}$$

where ρ and μ are the equivalent density and viscosity of the bulk phase fluid, respectively, and F_s is the surface tension force.

Eq. (9) represents a common transport equation with variable density and viscosity. The equivalent density and viscosity are derived from the volume fraction of the fluid:

$$\rho=\sum_{a=1}^{N_p}r_a\rho_a \tag{10}$$

$$\mu=\sum_{a=1}^{N_p}r_a\mu_a \tag{11}$$

where, r_a, ρ_a and μ_a are the volume fraction, density, and viscosity of fluid a, respectively, and N_p is the number of immiscible phases.

The continuity equation follows:

$$\frac{\partial \rho}{\partial t}+\nabla\cdot(\rho\boldsymbol{u})=0 \tag{12}$$

The sum of volume fractions is one in immiscible multiphase flows. Eq. (13) represents the volume conservation equation for incompressible fluids:

$$\sum_a\nabla\cdot(r_a\cdot\boldsymbol{u})=0 \tag{13}$$

In multiphase multicomponent flows, the transport equation of mass fraction of components in the mixture fluid consisting of CO_2 and oil is similar to that of multicomponent flows:

$$\frac{\partial}{\partial t}(r_b\rho_b\varphi_{bi})+\frac{\partial}{\partial x}(r_b\rho_b\boldsymbol{u}\varphi_{bi})=\frac{\partial}{\partial x}\left(\alpha\frac{\partial\varphi_{bi}}{\partial x}\right) \tag{14}$$

where r_b and ρ_b are the volume fraction and density of the mixture fluid b, respectively, and φ_{bi} is the mass fractions of components i in the mixture fluid.

The surface tension model employed is the continuum surface force model, which treats surface tension as a volume force concentrated at the interface. The wall adhesion is described using a contact angle. Furthermore, the interfacial transfer of momentum and mass is directly dependent on the contact surface area between the two phases. This is characterized by the interfacial area per unit volume between the phases (i.e., interfacial area density). The interfacial area density can be obtained by solving the volume fraction gradient, which describes the intensity of the interface variation.

4.4. Solution and simulation schemes

The developed multiphase multicomponent flow model is integrated into the CFX solver manager. For the equation solutions, an implicit time-stepping scheme, the second-order backward Euler method, is employed for transient calculations. A high-resolution scheme is used to discretize convection terms, with a preference for higher-order schemes to enforce the boundedness criterion (Hui et al., 2018). In regions where sharp gradient changes occur, this method automatically switches to a

first-order scheme to prevent overshoots and undershoots, thereby ensuring robustness. In addition, a compressive scheme is used for the volume fraction advection, with the interface compression level set to two to obtain a sharp interface.

Miscible and immiscible flow processes are separately validated to ensure the reliability of the numerical model. In combination with the slug flow microfluidic experiments conducted by Garstecki et al. (2006), immiscible flow simulations are performed under the same conditions for comparison. The simulated results for the slug volume and length under different injection conditions correspond well to the experimental results (Fig. 5 (a)). For verification of CO_2-oil dissolution, the diffusion process of CO_2 and oil is simulated within a closed space. The distribution of CO_2 concentration follows a Gaussian distribution, which is consistent with the predictions of Fick's law (Fig. 5 (b)). To verify the validity of the multiphase multicomponent flow process, the initial conditions shown in Fig. 5 (c) are set. Along the displacement direction, the fracture sequentially contains CO_2 and oil phases, with the water phase injected from the left side at a constant velocity. During the displacement process, convection-diffusion occurs between CO_2 and oil, while the flow between water and the mixture fluid is immiscible. Before CO_2 breakthrough, the average density of multiphase multicomponent fluids within the domain can be calculated based on the mass variation. In addition, water saturation can be calculated based on the volume of the injected water before the water breakthrough. Fig. 5 (d) demonstrates that the theoretically calculated average density and water volume fraction are in good agreement with the simulation results.

A subdomain with a size of 200 voxels is cropped for simulations (Fig. 6 (a)). To solve the multiphase multicomponent flow simulations, the fracture structure must be discretized. Tetrahedral grids are generated to describe the complex pore topology, and the resulting smooth surface ensures the rationality of interfacial tension calculations. Mesh models containing approximately 150,000, 300,000, 1,000,000, and 1,500,000 elements are generated to perform mesh sensitivity analysis for multiphase multicomponent flow simulations. The variation in outlet mass flow is compared across different grid resolutions. Changes in mass flow reflect detailed information on miscible and immiscible flow dynamics within fractures. As displayed in Fig. 6 (b), coarse models introduce significant errors in predicting breakthrough events and mass flow rates. In contrast, mesh models with 1,000,000 and 1,500,000 elements yield nearly identical mass flow rate predictions. Therefore, the mesh model with 1,000,000 elements is utilized for subsequent simulations.

Two types of schemes are designed to explore the dissolution between CO_2 and oil (Fig. 6 (c)). Table 2 lists the simulation scheme. The first scenario involves CO_2-oil miscible flows (Cases 1–4), with displacement processes conducted at four different injection velocities of CO_2. The CO_2 injection volume is approximately 1.5 PV, with a primary focus on analyzing the effects of convection and diffusion on the displacement process. The second scenario involves multiphase multicomponent water-CO_2-oil flows (Cases 5–8). Since CO_2 tends to flow along preferential pathways in the absence of capillary effect, CO_2 injection seriously leads to resource waste and is expensive in practical applications. Therefore, pre-injecting CO_2 into the oil-saturated fracture network, followed by water flooding, may potentially enhance the displacement efficiency. Four specific cases are designed (Table 2), with Case 5 serving as the control group to investigate the effects of different conditions on CO_2 dissolution. The impacts of CO_2 volume (Case 6), wettability (Case 7), and water injection velocity (Case 8) on CO_2 dissolution are analyzed. Considering that total organic carbon content and temperature influence rock wettability (Pan et al., 2020), simulations are conducted at contact angles of 30° and 80°, respectively. The injection process is divided into a pretreatment stage and a waterflooding stage. During the pretreatment stage, CO_2 is injected at a rate of 0.005 m/s with varying volumes. Subsequently, approximately 1.2 PV of water is injected to investigate the factors that influence CO_2 dissolution. These numerical models use the boundaries of velocity inlets and pressure outlets, with an outlet pressure set to 0. The wall properties are configured to no-slip conditions, and wall adhesion is taken into account by setting a contact angle for water and the mixture fluid. The displacement time is determined on the basis of the velocity and volume

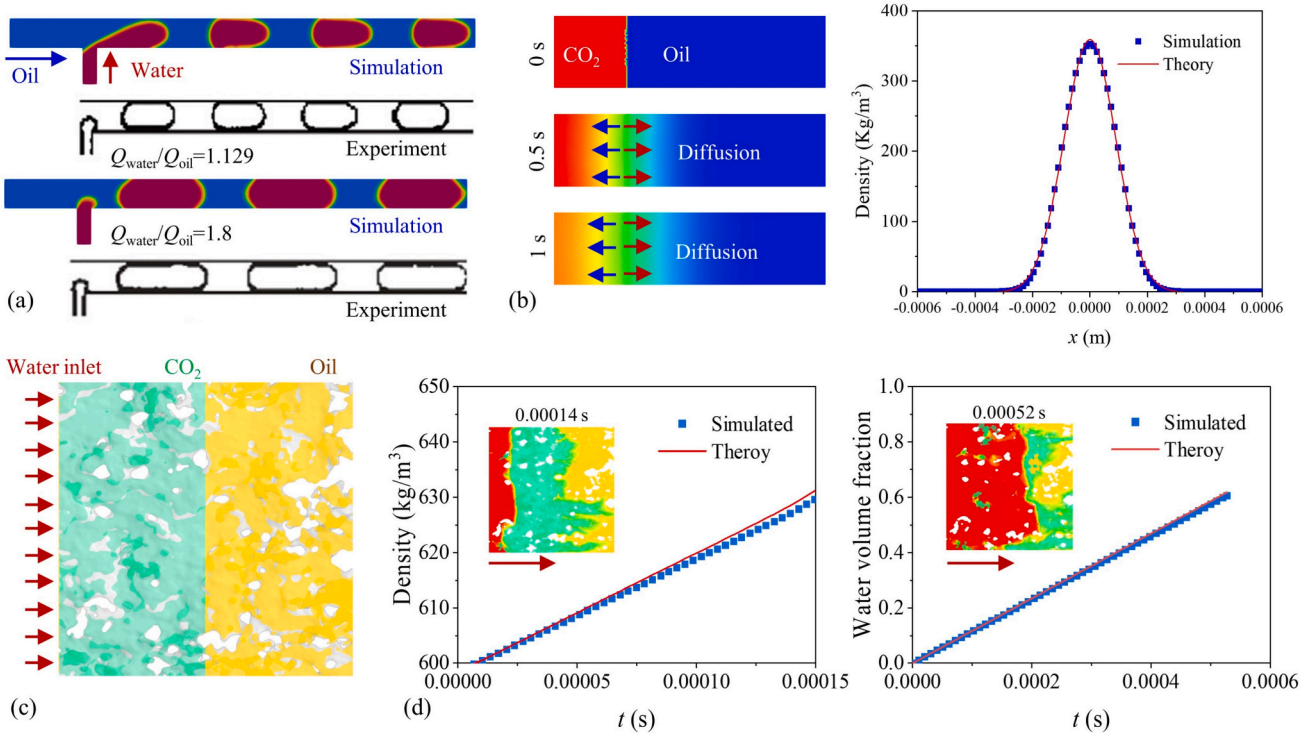

Fig. 5. Verification of the numerical model. (a) Immiscible and (b) miscible flow simulations verified by microfluidic experiments and Fick diffusion. (c) Configuration for the multiphase multicomponent flow. (d) Verification of density and water volume fraction.

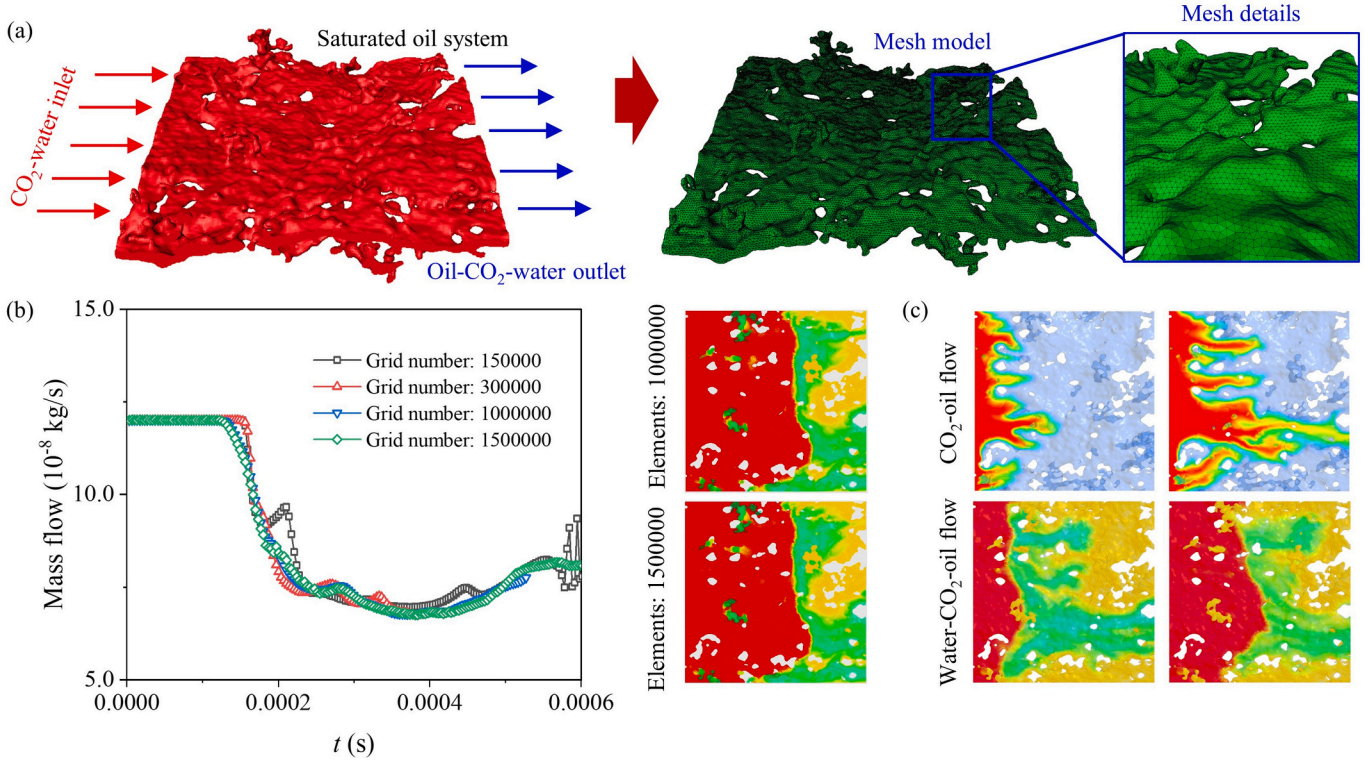

Fig. 6. Establishment of the numerical model. (a) Fracture structure for simulation. (b) Mesh sensitivity analysis. (c) Two types of simulation schemes.

Table 2
Simulation schemes.

Cases	Injected fluids	Velocity (m/s)	Contact angle (°)
1	1.5 PV CO_2	0.001	/
2	1.5 PV CO_2	0.005	/
3	1.5 PV CO_2	0.01	/
4	1.5 PV CO_2	0.05	/
5	0.1 PV CO_2 and 1.2 PV water	0.005	30
6	0.3 PV CO_2 and 1.2 PV water	0.005	30
7	0.1 PV CO_2 and 1.2 PV water	0.005	80
8	0.1 PV CO_2 and 1.2 PV water	0.05	30

of the injected fluid. The time step is controlled by the courant number, ensuring that the maximum distance traveled by the fluid flow in each time step is significantly smaller than the grid size. In the simulation, the maximum courant number is around 0.1, and the average courant number is less than 0.01. On the basis of the above simulations, the sequestration and displacement efficiency under different injection conditions are evaluated.

The density and viscosity parameters for the water-CO_2-oil flow are displayed in Table 3. Due to the extremely high viscosity of crude oil at ambient temperature, its viscosity is experimentally measured to be 1.4 mPa·s at the reservoir temperature. Additionally, the density and viscosity of supercritical CO_2 vary significantly and are strongly influenced by temperature and pressure. To highlight the effect of CO_2 dissolution on reducing the density and viscosity of crude oil, the density of CO_2 is established at 400 kg/m^3 and its viscosity at 0.05 mPa·s. The flow between the water and the mixture fluid is immiscible, with an interfacial tension of 0.048 N/m. The dissolution of supercritical CO_2 and oil is controlled by defining the diffusion coefficient. The diffusion coefficient of CO_2-oil increases with increasing temperature and pressure. To restore CO_2-oil flow under reservoir conditions, the diffusion coefficient of 2×10^{-9} m^2/s, as experimentally determined by Li et al. (2016), is used.

Table 3
Fluid properties.

Fluids	Components	Density (kg/m^3)	Viscosity (mPa·s)
Mixture	CO_2	400	0.05
	Oil	800	1.40
Water	Water	1000	1.00

5. Results and discussion

5.1. CO_2-oil miscible displacement processes

In the CO_2-oil displacement process, 1.5 PV of CO_2 is injected into the oil-saturated fracture network. Fig. 7 displays the CO_2 mass fraction and the fluid pressure distribution characteristics of Case 1 (0.001 m/s) and Case 4 (0.05 m/s) at different injection rates. Due to the miscible flow between CO_2 and oil, the fingering phenomenon becomes significant as CO_2 injection amounts increase. Significantly, CO_2 flows rapidly along the preferential pathways and gradually diffuses into poorly connected regions without the effect of interfacial tension. As displacement progresses, the injected CO_2 reduces the fluid pressure. Fluid pressure decreases from the inlet to the outlet and drops rapidly after CO_2 breaks through the outlet. In addition, the displacement patterns differ at various injection rates. This is because the injection rate affects the convection and diffusion intensity between CO_2 and oil, which can be described by the Peclet number. The corresponding Peclet numbers at different velocities (0.001, 0.005, 0.01, 0.05 m/s) are 2.05, 10.25, 20.5, and 102.5, respectively.

To quantitatively describe the CO_2-oil miscible flow characteristics at different injection rates, the changes in mass flow rate, pressure, mass fraction, mixture density, and viscosity are extracted during the displacement process. The injection rate positively correlates with the outlet mass flow rate (Fig. 8 (a)). In the initial stage of displacement, the outlet mass flow is constant, indicating that only the oil component flows out of the outlet. Subsequently, the mass flow rate decreases,

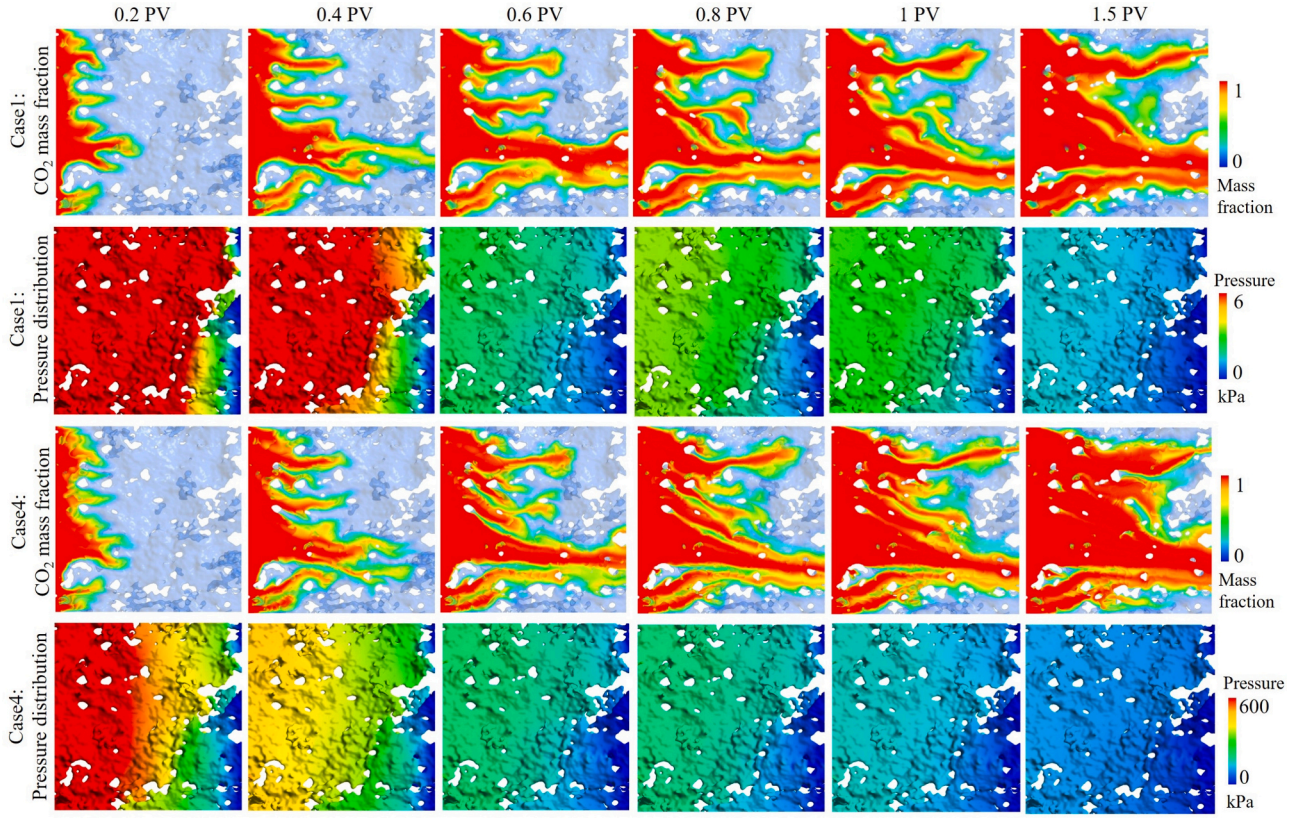

Fig. 7. Mass fraction and density distribution in the process of CO_2 flooding.

indicating that the CO_2 breaks through the outlet. The CO_2 breakthrough events in Cases 1–3 are found to be relatively consistent, with the breakthrough occurring after approximately 0.36 PV of CO_2 is injected. However, the breakthrough event occurs after the injection of 0.44 PV of CO_2 when the injection rate increases to 0.05 m/s. This means that the high injection rate expands the CO_2 sweep area in the fracture network. In addition, during the brief period of breakthrough, outlet mass flow declined rapidly, indicating that a large volume of bulk CO_2 flows out through the dominant channels. After the breakthrough event, the mass flow rate may increase to a certain extent, and the flow attenuation rate is significantly reduced. This indicates that the proportion of oil in the flowing mixture fluid increases after the breakthrough, and CO_2 dissolves in the oil under convection-diffusion.

Before the breakthrough event, convection is stronger than diffusion effects. CO_2 mass fraction exhibits an upward trend, with the increase rate gradually accelerating (Fig. 8 (b)). After the breakthrough, a large amount of CO_2 flows out, and the mass fraction of CO_2 slowly increases under the action of diffusion. In addition, the injection rate is positively correlated with the CO_2 mass fraction, indicating that the higher velocity in the fracture system enhances the convection-diffusion effect between CO_2 and oil components, resulting in significant improvements in mass transfer. Especially when the injection velocity is 0.05 m /s, the mass fraction increases significantly. This is because a substantial increase in injection velocity increases the CO_2 sweep area (Fig. 7) and enhances the interaction between CO_2 and oil, promoting mass transfer.

The injected CO_2 reduces the density and viscosity of the mixture fluid. The density decreases linearly before the breakthrough, and the decrease trend slows down rapidly after the breakthrough (Fig. 8 (c)). The viscosity of the mixture fluid exhibits a trend opposite to that of the CO_2 mass fraction (Fig. 8 (d)), according to the calculation principle for mixture viscosity (Eq. 14). The higher the injection velocity, the more obvious the decrease in density and viscosity of the mixture fluid. Depending on changes in outlet mass flow, the injection pressure gradually decreases during the displacement process (Fig. 8 (e)). After the breakthrough, due to the dissolution of CO_2, the pressure slightly increases and then decreases slowly. As expected, the injection pressure is positively correlated with the flow rate. The increase in injection pressure enhances the displacement efficiency, corresponding to a high CO_2 mass fraction. Fluid pressure is slightly lower than the injection pressure with a consistent variation trend (Fig. 8 (f)).

5.2. *Water-CO_2-oil displacement process*

Obviously, a large amount of CO_2 flows out along the preferential pathways without the influence of capillary forces, resulting in resource waste (Fig. 7). Therefore, initially injecting CO_2 to dissolve in the oil, followed by water flooding, may reduce the fingering phenomenon due to the capillary effects between the water and the mixture fluid, thereby enhancing the dissolution and displacement efficiency. As displayed in Fig. 9, there are significant density differences among water, oil, and CO_2 in the multiphase multicomponent system. A distinct interface exists between the water and the mixture fluid, while CO_2 and oil are miscible. It is found that the water flow is controlled by capillary forces and easily forms stable displacement patterns. This reduces CO_2 flow along preferential pathways and enhances CO_2 sweep efficiency. Additionally, a density transition region between CO_2 and oil indicates that some CO_2 dissolves in oil during the displacement process. Dissolved CO_2 reduces the density and viscosity of the oil. In reality, the amount of CO_2, contact angle, and water injection rate will affect the variation of pressure, interface dynamics, and mass flow, ultimately leading to different CO_2-oil dissolution characteristics (Figs. 10 and 11).

The displacement patterns between water and the mixture fluid are basically the same in fracture networks containing 0.1 PV and 0.3 PV of CO_2 (Cases 5 and 6 in Fig. 9). Due to the fingering phenomenon, CO_2 breaks through the outlet prematurely in the model with a high CO_2 content (Case 6), resulting in a rapid decrease in the mass flow of

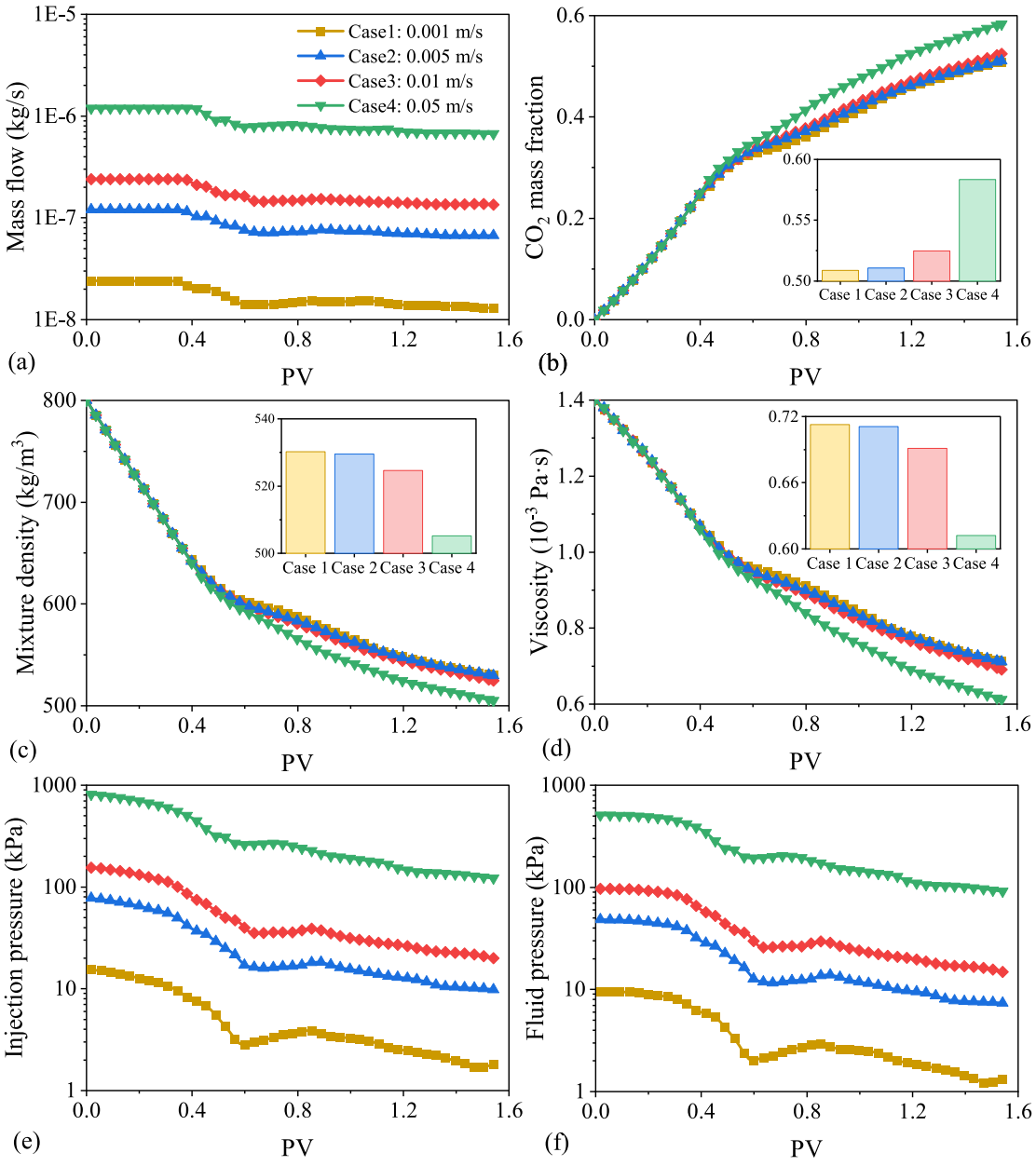

Fig. 8. CO_2 flooding parameters. (a) Outlet mass flow, (b) CO_2 mass fraction, (c) mixture density and (d) viscosity, (e) injection pressure, and (f) fluid pressure.

mixture fluid and a low storage efficiency. During the water flooding process, CO_2 breaks through the outlet after injecting 0.27 PV and 0.05 PV of water in Case 5 and Case 6, respectively. Additionally, water breaks through the outlet after injecting 0.63 PV of water in the two cases. Subsequently, the water mass flow increases rapidly, while the mass flow of the mixture fluid declines sharply (Fig. 10 (a) and (b)). Increased CO_2 volume leads to a significant decrease in displacement pressure and fluid pressure (Fig. 11 (a) and (b)). The initial displacement pressure in the model with 0.3 PV of CO_2 is reduced from 61.4 kPa to 43.4 kPa, compared to the model with 0.1 PV of CO_2. As the displacement progresses, bulk CO_2 and dissolved CO_2 are displaced, and the water injection pressures in the two cases gradually approach. The changes in the contact area of water and mixture fluid are consistent, indicating that the interface dynamics are similar (Fig. 11 (c)). As expected, the CO_2 mass fraction is higher during water flooding in the model with a higher CO_2 content. The CO_2 mass fraction increases during water flooding and gradually decreases when CO_2 breaks through the outlet. After the water flooding, the CO_2 mass fractions for Case 5 and Case 6 are 13.6 % and 15.5 %, respectively (Fig. 11 (d)). The variations in the density and viscosity of the mixture fluid are opposite to the variations in CO_2 mass fraction. Increased CO_2 amount reduces the density and viscosity of the mixture fluid during water flooding (Fig. 11 (e) and (f)).

The flow characteristics are compared under strongly and weakly hydrophilic conditions (Cases 5 and 7 in Fig. 9). Due to the reduced constraint of the pore surface on water, the water flow along the preferential pathways is pronounced under weakly hydrophilic conditions. In the two cases, CO_2 breaks through the outlet after injecting 0.27 PV of water. However, water breaks through the outlet earlier under weakly hydrophilic conditions, and the mass flow of the mixture fluid decreases sharply, indicating unsatisfactory displacement performance (Fig. 10 (c)). Since the capillary pressure under the weakly hydrophilic condition is smaller, the water injection pressure and fluid pressure are higher compared to strongly hydrophilic conditions (Fig. 11 (a) and (b)). Consequently, the water injection pressure in Case 7 increases by 13 kPa compared to Case 5. Due to the constraint of contact angle, the contact

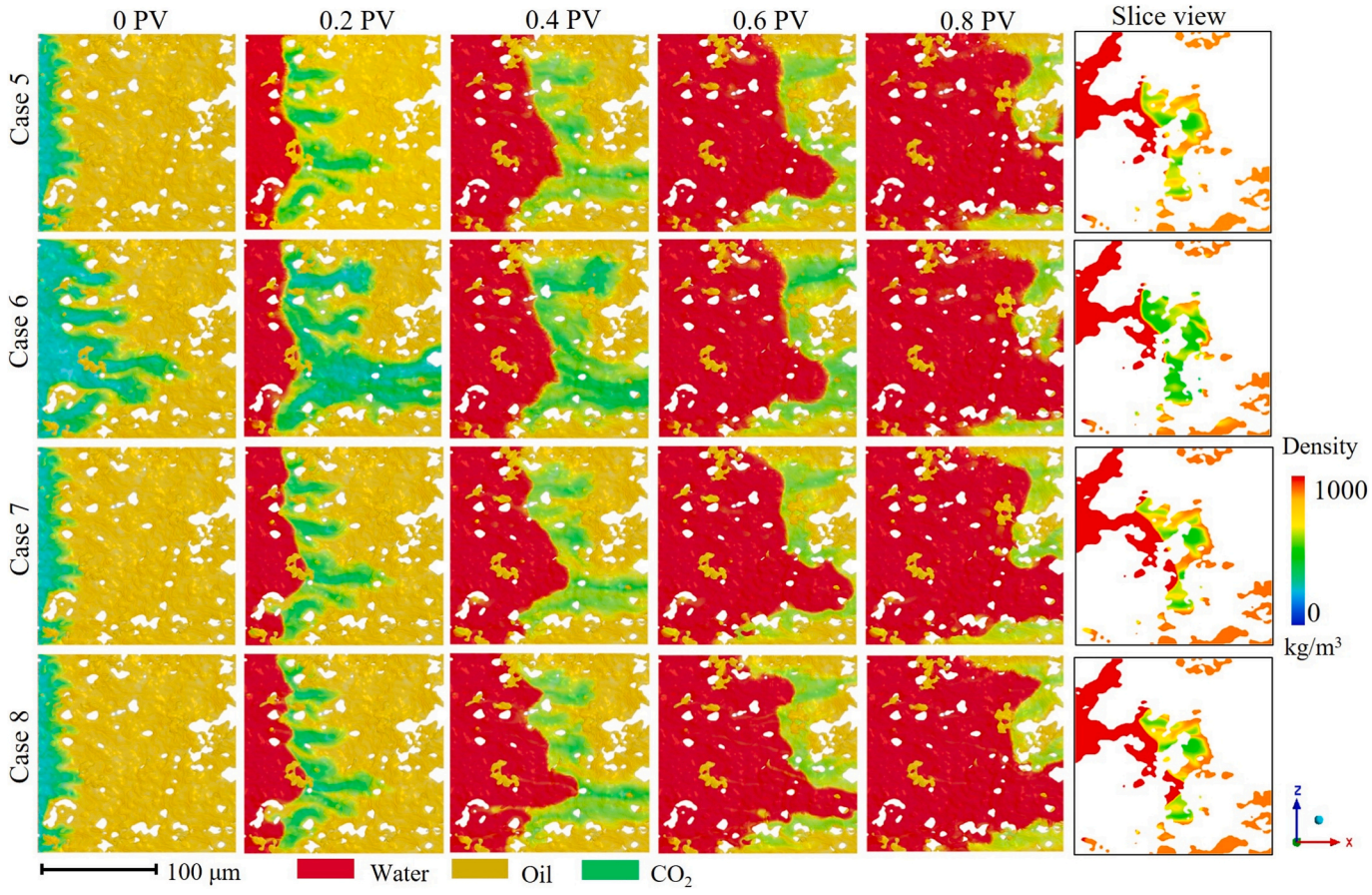

Fig. 9. Density distribution for water-oil-CO_2 multiphase multicomponent flow under four cases.

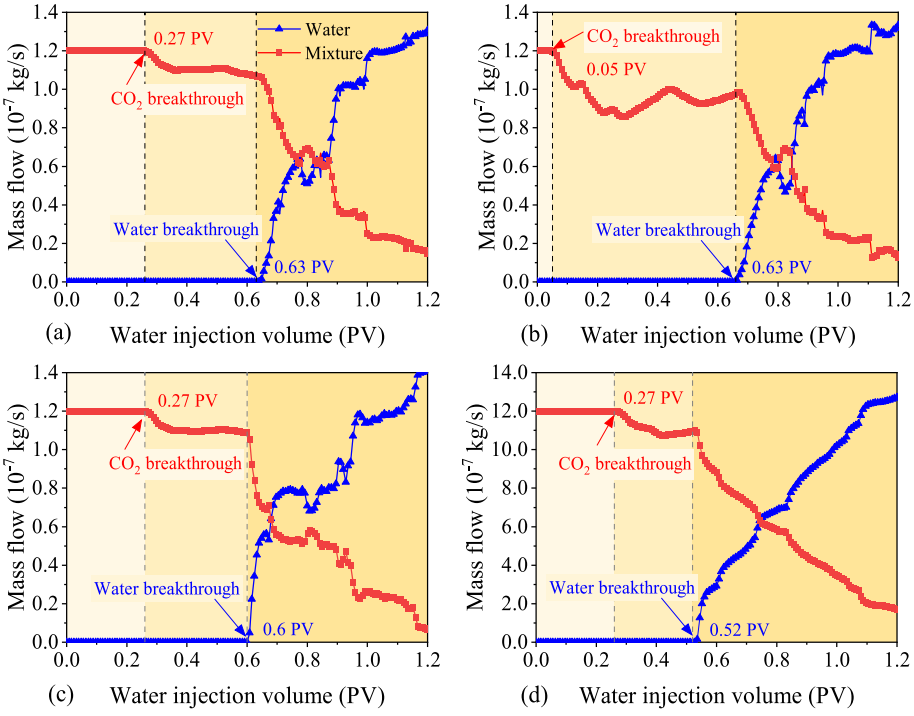

Fig. 10. Outlet mass flow characteristics during water-CO_2-oil displacement. (a) Case 5; (b) Case 6; (c) Case 7; (d) Case 8.

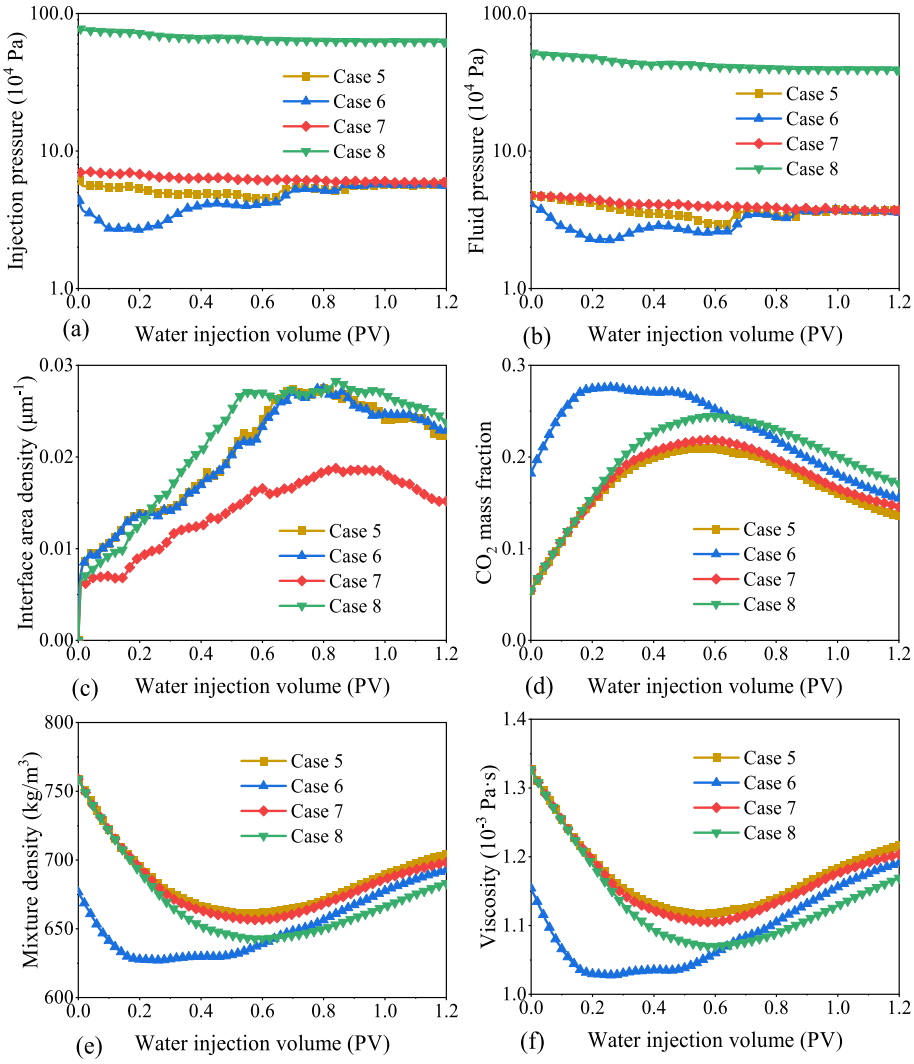

Fig. 11. Dynamic parameters of water-CO_2-oil displacement. The change in (a) injection pressure, (b) fluid pressure, (c) interface area density, (d) CO_2 mass fraction, (e) mixture density, and (f) viscosity.

area between water and the mixture fluid is smaller under weakly hydrophilic conditions (Fig. 11 (c)). This weakens the interactions of injected water with the mixture fluid and is not conducive to EOR. In addition, the changes in CO_2 mass fraction (Fig. 11 (d)), density (Fig. 11 (e)), and viscosity (Fig. 11 (f)) of the mixture fluid during the water flooding are basically the same in Case 5 and Case 7.

Variation in injection velocity during waterflooding affects the interaction between capillary and viscous forces in immiscible systems, as well as the interaction between convection and diffusion in miscible systems. The viscous force has a significant effect under high water injection velocity, and the corresponding fingering phenomenon is obvious (Cases 5 and 8 in Fig. 9). This causes the wetting fluid to break through the outlet earlier. In Case 8, the water breaks through the outlet after 0.52 PV of water is injected (Fig. 10 (d)). Due to the effect of viscous forces, the fluctuation of mass flow is not significant. The mass flow of the mixture fluid decreases slowly after breakthrough, indicating high CO_2 sequestration and oil displacement efficiencies. Additionally, the increase in injection velocity leads to an increase in the injection pressure and the fluid pressure (Fig. 11 (a) and (b)). It is noted that the high injection velocity causes interface distortion, increasing the interfacial area between water and the mixture fluid (Fig. 11 (c)) and significantly enhancing fluid interactions. The high injection velocity and complex interface dynamics enhance the dissolution of CO_2. Therefore, the CO_2 mass fraction is higher in Case 8 (Fig. 11 (d)). Due to the strong solubility, the density and viscosity of the mixture fluid are the lowest after water flooding (Fig. 11 (e) and (f)).

5.3. Evaluation of displacement and sequestration efficiency

The processes of CO_2 flooding and CO_2 injection followed by water flooding are compared. Variation in outlet mass flow reflects the microscopic dynamic production process. A rapid decline indicates that a large amount of CO_2 is flowing out, signifying poor sequestration efficiency. Conversely, a higher mass flow indicates a large oil content in the mixture fluid, which corresponds to enhanced displacement efficiency. Fig. 12 (a) compares the variation in outlet mass flow between CO_2 flooding and CO_2 injection followed by water flooding under the same injection rate. Before the CO_2 breakthrough, the outlet mass flow rate remains constant. However, a significant difference in outlet mass flow is observed after the CO_2 breakthrough. For CO_2 flooding, mass flow decreases rapidly, indicating that injected CO_2 flows out quickly along dominant pathways. Following the injection of 0.6 PV of CO_2, the outlet mass flow drops from 1.2×10^{-7} kg/s to 7.35×10^{-8} kg/s, representing a 38 % reduction. Subsequently, CO_2 continues to dissolve in the oil, expanding the sweep area, and the mass flow decreases gradually. However, a large amount of CO_2 needs to be injected to achieve satisfactory displacement efficiency. It is worth noting that during CO_2 injection followed by water flooding, the outlet mass flow decreases

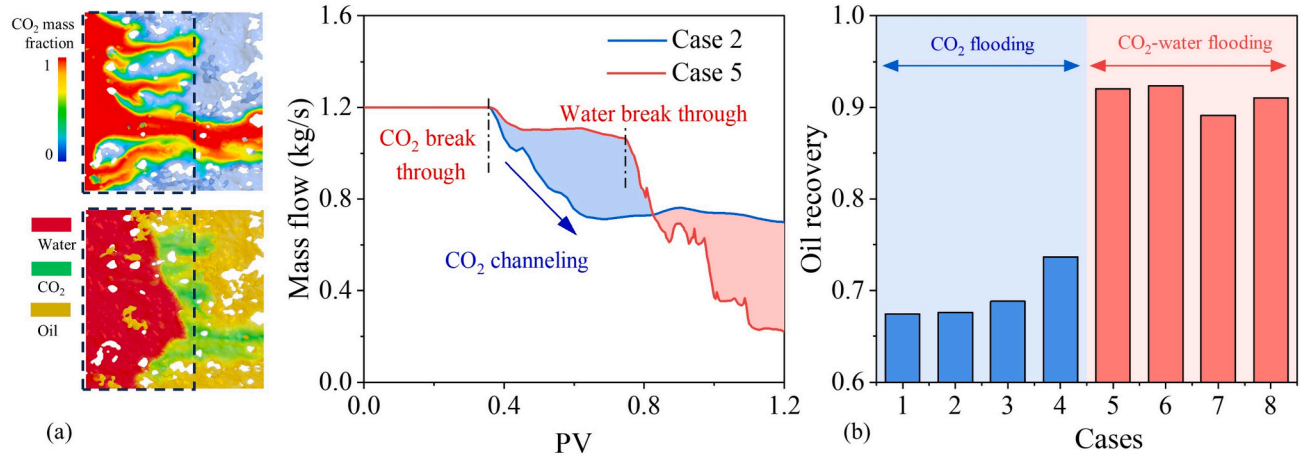

Fig. 12. Comparison of simulation results of CO_2 flooding and CO_2 injection followed by water flooding. (a) Flow characteristics. (b) Oil recovery.

slowly. After CO_2 breakthrough, the mass flow decreases from 1.2×10^{-7} kg/s to 1.11×10^{-7} kg/s, representing only a 7.5 % reduction. Due to the strong water-wall interactions, capillary forces promote the liquid flow within microchannels while inhibiting the flow process in large pore bodies, which facilitates the formation of a stable displacement front. Therefore, injecting water into the fracture network can weaken the CO_2 channeling and enhance the dissolution of CO_2.

Differences in oil recovery are observed under different injection conditions (Fig. 12 (b)). Injecting CO_2 followed by water flooding, significantly enhances the recovery compared to CO_2 flooding. During the CO_2 flooding process, oil recovery is about 70 % for Cases 1–3. With increasing injection velocity and pressure, oil recovery increases to 73.7 % at an injection velocity of 0.05 m/s. Pre-injecting CO_2 into the fracture network to reduce the density and viscosity of the oil, followed by water flooding, enhances the oil recovery to approximately 90 %. This is because CO_2 with low viscosity and density exhibits high mobility. During miscible displacement, CO_2 channels through fractures, limiting the displacement efficiency. In contrast, by injecting CO_2 followed by water flooding, the injected water can coordinate the displacement process in pores with different sizes due to capillary effects, weaken the CO_2 channeling along fractures, and form a stable displacement front, thus expanding the sweep area.

Oil recovery and CO_2 storage efficiency are further analyzed among the cases of water flooding following CO_2 injection (Cases 5–8). Due to

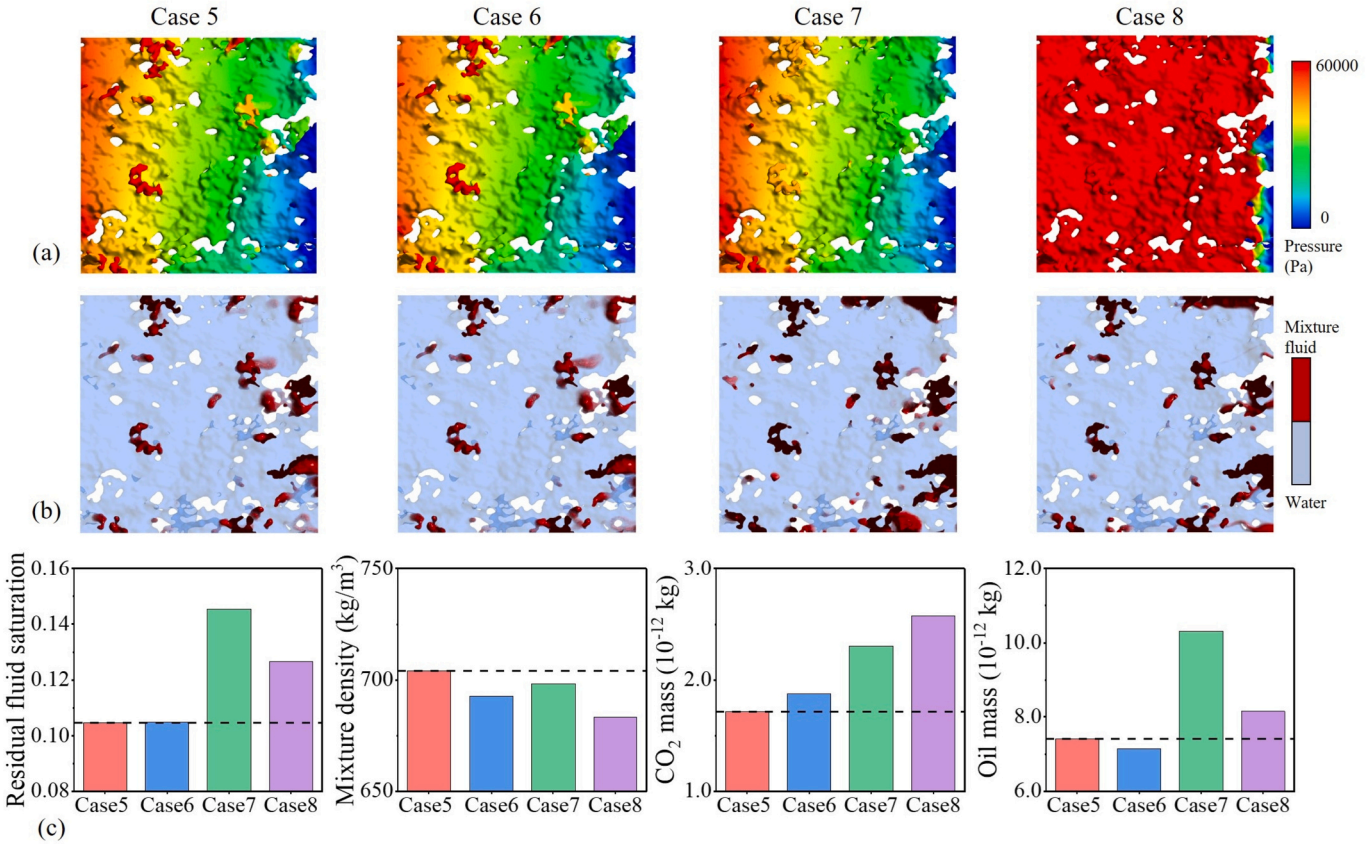

Fig. 13. Evaluation of oil recovery and CO_2 sequestration efficiency. (a) Pressure distribution and (b) residual fluid distribution after water flooding. (c) Fluid parameters after water flooding.

continuous water injection, the fluid pressure gradually decreases from the inlet to the outlet (Fig. 13 (a)). The pore space where the residual oil is distributed corresponds to a higher fluid pressure. Since the simulation neglects the effect of CO_2 content on interfacial tension and wettability of the mixture fluid, the residual fluid distributions are nearly consistent in Case 5 and Case 6, with the mixture fluid trapped in blind-end pores (Fig. 13 (b)). However, the increased CO_2 amount enhances dissolution and reduces oil density and viscosity, corresponding to the highest oil recovery (Fig. 13 (c)). Under weakly hydrophilic conditions, the contact area between water and the mixture fluid is smaller, limiting the sweep area of water. Due to the weakened capillary forces, the volume of residual fluids in blind-end pores increases, and some residual fluids are attached to the rough fracture surfaces (Fig. 13 (b)). Although the snap-off of non-wetting fluid occurs in the pore throats with a large aspect ratio under strong hydrophilic conditions, this phenomenon is not obvious in fracture structures. Therefore, the residual fluid saturation is the highest, and the recovery is the lowest under the weakly hydrophilic condition (Fig. 13 (c)). It is noticed that the high injection velocity corresponds to the highest CO_2 storage and lower residual oil content (Fig. 13 (c)) due to enhanced CO_2 dissolution. Additionally, the outlet mass flow in Case 8 decreases slowly during the water flooding process (Fig. 10 (d)), indicating effective oil production and CO_2 sequestration capability.

Based on simulation studies, several strategies are suggested to enhance oil recovery and CO_2 sequestration efficiency. In reservoirs with developed fractures, the CO_2 WAG displacement exhibits superior performance compared to CO_2 flooding. The CO_2 injection rates and volume affect the dissolution efficiency. Increasing the CO_2 injection rate enhances contact with oil and accelerates dissolution. However, excessive CO_2 injection can result in a premature breakthrough, which reduces sequestration efficiency. Therefore, following high-rate CO_2 injection, a shut-in period can be implemented to allow CO_2 to fully dissolve in the oil, reducing the density and viscosity of the crude oil. Wettability and injection rate influence the subsequent waterflooding process. Hydrophilic surfaces facilitate the expansion of the sweep area, leading to a stable displacement process. Furthermore, increasing the injection rate helps enhance both recovery and sequestration efficiency.

6. Conclusions

This work develops a pore-scale model for water-CO_2-oil flow within shale fractures to explore microscopic mechanisms underlying CO_2-enhanced recovery and sequestration efficiency. The processes of CO_2 miscible flooding and water flooding following CO_2 injection are simulated, and the effects of key factors on CO_2 dissolution and oil recovery are analyzed. The following conclusions are drawn:

(1) During CO_2 flooding, the injected CO_2 tends to flow along preferential pathways and gradually diffuses to poorly connected areas. Injected CO_2 reduces the fluid pressure, and the injection pressure decreases as the CO_2 injection volume increases. Increasing the injection velocity enhances interactions between CO_2 and oil components, thereby reducing the density and viscosity of oil.

(2) For the process of water flooding following CO_2 injection, stable displacement patterns are formed between the water and the mixture fluid. A higher CO_2 content increases the CO_2 mass fraction but causes premature breakthrough. A large contact angle leads to the entrapment of non-wetting fluids in blind-end pores and regions with poor connectivity. However, increasing the water injection rate enlarges the contact area between the water and the mixture fluid, enhancing CO_2 dissolution.

(3) Water flooding following CO_2 injection in shale fractures increases oil recovery by approximately 20 % compared to CO_2 flooding. During CO_2 flooding, the outlet mass flow decreases by 38 % after CO_2 breakthrough. In contrast, the mass flow decreases by only 7.5 % during the water-CO_2-oil displacement. The outlet mass flow decays slowly at high water injection rates, corresponding to satisfactory displacement and sequestration effects.

CRediT authorship contribution statement

Xiangjie Qin: Writing – review & editing, Writing – original draft, Software, Methodology, Investigation. **Han Wang:** Writing – review & editing, Visualization, Software, Funding acquisition. **Yuxuan Xia:** Writing – review & editing, Supervision, Funding acquisition, Conceptualization. **Xinghe Jiao:** Writing – review & editing, Supervision, Investigation. **Gang Wang:** Writing – review & editing, Software, Formal analysis. **Jianchao Cai:** Writing – review & editing, Methodology, Funding acquisition, Conceptualization.

Declaration of competing interest

The authors declare that they have no known competing financial interests or personal relationships that could have appeared to influence the work reported in this paper.

Acknowledgments

This work was supported by National Natural Science Foundation of China (Nos. 42172159, 52404048), China Postdoctoral Science Foundation (No. 2023M743870), and Postdoctoral Fellowship Program of CPSF (No. GZB20230864).

Data availability

Data will be made available on request.

References

Afzali, S., Rezaei, N., Zendehboudi, S., Chatzis, I., 2022. Computational fluid dynamic simulation of multi-phase flow in fractured porous media during water-alternating-gas injection process. J. Hydrol. 610, 127852. https://doi.org/10.1016/j.jhydrol.2022.127852.

Asemani, M., Rezaei, A., 2022. Chapter 9 - Combination of chemical methods. In: Hemmati-Sarapardeh, A., Schaffie, M., Ranjbar, M., Dong, M., Li, Z. (Eds.), Chemical Methods. Gulf Professional Publishing, pp. 401–431. https://doi.org/10.1016/B978-0-12-821931-7.00005-5.

Behnoud, P., Khorsand Movaghar, M.R., Sabooniha, E., 2023. Numerical analysis of pore-scale CO2-EOR at near-miscible flow condition to perceive the displacement mechanism. Sci. Rep. 13, 12632. https://doi.org/10.1038/s41598-023-39706-1.

Chen, S., Liu, X., Cui, Y., Zhao, X., Zhang, J., 2017. Palaeogene structural evolution of Dongying Depression, Bohai Bay Basin, NE China. Int. Geol. Rev. 59, 259–273. https://doi.org/10.1080/00206814.2016.1223559.

Cai, J., Qin, X., Wang, H., Xia, Y., Zou, S., 2025. Pore-scale investigation of forced imbibition in porous rocks through interface curvature and pore topology analysis. J. Rock Mech. Geotech. Eng. 17 (1), 245–257. https://doi.org/10.1016/j.jrmge.2024.02.047.

Chen, L., He, A., Zhao, J., Kang, Q., Li, Z.-Y., Carmeliet, J., Shikazono, N., Tao, W.-Q., 2022. Pore-scale modeling of complex transport phenomena in porous media. Prog. Energy Combust. Sci. 88, 100968. https://doi.org/10.1016/j.pecs.2021.100968.

Chowdhury, S., Rakesh, M., Medhi, S., Trivedi, J., Sangwai, J.S., 2022. Pore-scale flow simulation of supercritical CO2 and oil flow for simultaneous CO2 geo-sequestration and enhanced oil recovery. Environ. Sci. Pollut. Res. 29, 76003–76025. https://doi.org/10.1007/s11356-022-21217-7.

Davoodi, S., Al-Shargabi, M., Wood, D.A., Rukavishnikov, V.S., Minaev, K.M., 2023. Review of technological progress in carbon dioxide capture, storage, and utilization. Gas Sci. Eng. 117, 205070. https://doi.org/10.1016/j.jgsce.2023.205070.

Edwards, R.W.J., Celia, M.A., 2018. Infrastructure to enable deployment of carbon capture, utilization, and storage in the United States. Proc. Natl. Acad. Sci. USA 115, E8815–E8824. https://doi.org/10.1073/pnas.1806504115.

Garstecki, P., Fuerstman, M.J., Stone, H.A., Whitesides, G.M., 2006. Formation of droplets and bubbles in a microfluidic T-junction—scaling and mechanism of break-up. Lab Chip 6, 437–446. https://doi.org/10.1039/B510841A.

Han, X., Song, Z., Deng, S., Li, B., Li, P., Lan, Y., Song, Y., Zhang, L., Zhang, K., Zhang, Y., 2024. Multiphase behavior and fluid flow of oil–CO2–water in shale oil reservoirs: Implication for CO2-water-alternating-gas huff-n-puff. Phys. Fluids 36, 063310. https://doi.org/10.1063/5.0213861.

Hao, Y., Li, Z., Su, Y., Kong, C., Chen, H., Meng, Y., 2022. Experimental investigation of CO2 storage and oil production of different CO2 injection methods at pore-scale and core-scale. Energy 254, 124349. https://doi.org/10.1016/j.energy.2022.124349.
Hui, D., Zhang, G.Y., Yu, D.P., Sun, Z., Zong, Z., 2018. Numerical study of advection schemes for interface-capturing using gradient smoothing method. Numer. Heat Transf. B Fundam. 73, 242–261. https://doi.org/10.1080/10407790.2018.1462005.
Khurshid, I., Afgan, I., 2021. Geochemical investigation of CO2 injection in oil and gas reservoirs of middle east to estimate the formation damage and related oil recovery. Energies 14, 7676. https://doi.org/10.3390/en14227676.
Li, S., Li, Z., Dong, Q., 2016. Diffusion coefficients of supercritical CO2 in oil-saturated cores under low permeability reservoir conditions. J. CO2 Util. 14, 47–60. https://doi.org/10.1016/j.jcou.2016.02.002.
Li, Z., Liu, J., Su, Y., Fan, L., Hao, Y., Kanjibayi, B., Huang, L., Ren, S., Sun, Y., Liu, R., 2023. Influences of diffusion and advection on dynamic oil-CO2 mixing during CO2 EOR and storage process: Experimental study and numerical modeling at pore-scales. Energy 267, 126567. https://doi.org/10.1016/j.energy.2022.126567.
Liu, H., 2022. Exploration practice and prospect of shale oil in Jiyang depression. China Petrol. Explor. 27, 73–87. https://doi.org/10.3969/j.issn.1672-7703.2022.01.007.
Liu, B., Liu, W., Pan, Z., Yu, L., Xie, Z., Lv, G., Zhao, P., Chen, D., Fang, W., 2022. Supercritical CO2 breaking through a water bridge and enhancing shale oil recovery: a molecular dynamics simulation study. Energy Fuel 36, 7558–7568. https://doi.org/10.1021/acs.energyfuels.2c01547.
Liu, T., Jiang, Z., Jia, H., Wu, X., Yu, J., Zhao, B., Wei, S., 2023. Controlling factors of the gypsum-salt strata differences within two adjacent Eocene sags in the eastern Jiyang Depression, NE China and its hydrocarbon significance. Geoenergy Sci. Eng. 231, 212352. https://doi.org/10.1016/j.geoen.2023.212352.
Lu, T., Li, Z., Gu, Z., Du, L., 2023. Stability and enhanced oil recovery performance of CO2 in water emulsion: Experimental and molecular dynamic simulation study. Chem. Eng. J. 464, 142636. https://doi.org/10.1016/j.cej.2023.142636.
Ma, L., Song, M., Wang, Y., Wang, Y., Liu, H., 2023. Exploration progress of the paleogene in Jiyang depression, Bohai Bay Basin. Energy Geosci. 4, 42–50. https://doi.org/10.1016/j.engeos.2022.07.004.
Massarweh, O., Abushaikha, A.S., 2022. A review of recent developments in CO2 mobility control in enhanced oil recovery. Petroleum 8, 291–317. https://doi.org/10.1016/j.petlm.2021.05.002.
Nguyen, P., Carey, J.W., Viswanathan, H.S., Porter, M., 2018. Effectiveness of supercritical-CO2 and N2 huff-and-puff methods of enhanced oil recovery in shale fracture networks using microfluidic experiments. Appl. Energy 230, 160–174. https://doi.org/10.1016/j.apenergy.2018.08.098.
Pan, B., Li, Y., Zhang, M., Wang, X., Iglauer, S., 2020. Effect of total organic carbon (TOC) content on shale wettability at high pressure and high temperature conditions. J. Pet. Sci. Eng. 193, 107374. https://doi.org/10.1016/j.petrol.2020.107374.
Punetha, M., Khandekar, S., 2017. A CFD based modelling approach for predicting steam condensation in the presence of non-condensable gases. Nucl. Eng. Des. 324, 280–296. https://doi.org/10.1016/j.nucengdes.2017.09.007.
Qin, X., Cai, J., Wang, G., 2023. Pore-scale modeling of pore structure properties and wettability effect on permeability of low-rank coal. Int. J. Min. Sci. Technol. 33, 573–584. https://doi.org/10.1016/j.ijmst.2023.02.005.
Qin, X., Wu, J., Xia, Y., Wang, H., Cai, J., 2024. Multicomponent image-based modeling of water flow in heterogeneous wet shale nanopores. Energy 298, 131367. https://doi.org/10.1016/j.energy.2024.131367.
Sambo, C., Liu, N., Shaibu, R., Ahmed, A.A., Hashish, R.G., 2023. A technical review of CO2 for enhanced oil recovery in unconventional oil reservoirs. Geoenergy Sci. Eng. 221, 111185. https://doi.org/10.1016/j.petrol.2022.111185.
Shypul, O., Plankovskyy, S., Zaklinskyy, S., Pavlenko, O., Garin, V., 2022. Determination of the mass of gas in a reservoir at filling with a mixture component under the pressure. In: Nechyporuk, M., Pavlikov, V., Kritskiy, D. (Eds.), Integrated Computer Technologies in Mechanical Engineering. Springer International Publishing, Cham, pp. 166–177.
Song, W., Liu, F., Li, Y., Yang, Y., 2024a. Pore scale modeling of fluid transport in complex reservoirs: Multi-scale digital rock construction, flow experiments and simulation methods. Capillarity 11, 81–88. https://doi.org/10.46690/capi.2024.06.03.
Song, Y., Song, Z., Meng, Y., Chen, Z., Han, X., Feng, D., 2024b. Multi-phase behavior and pore-scale flow in medium-high maturity continental shale reservoirs with Oil, CO2, and water. Chem. Eng. J. 484, 149679. https://doi.org/10.1016/j.cej.2024.149679.
Tang, W.-Y., Sheng, J.J., Jiang, T.-X., 2023. Further discussion of CO2 huff-n-puff mechanisms in tight oil reservoirs based on NMR monitored fluids spatial distributions. Pet. Sci. 20, 350–361. https://doi.org/10.1016/j.petsci.2022.08.014.
Wang, Q., Yang, S., Lorinczi, P., Glover, P.W.J., Lei, H., 2020. Experimental investigation of oil recovery performance and permeability damage in multilayer reservoirs after CO2 and water–alternating-CO2 (CO2–WAG) flooding at miscible pressures. Energy Fuel 34, 624–636. https://doi.org/10.1021/acs.energyfuels.9b02786.
Wang, G., Qin, X., Han, D., Liu, Z., 2021. Study on seepage and deformation characteristics of coal microstructure by 3D reconstruction of CT images at high temperatures. Int. J. Min. Sci. Technol. 31, 175–185. https://doi.org/10.1016/j.ijmst.2020.11.003.
Wang, G., Chen, X., Wang, S., Chen, H., 2022a. Influence of fracture connectivity and shape on water seepage of low-rank coal based on CT 3D reconstruction. J. Nat. Gas Sci. Eng. 102, 104584. https://doi.org/10.1016/j.jngse.2022.104584.
Wang, H., Su, Y., Wang, W., 2022b. Improved lattice Boltzmann method to simulate liquid flow in nanoporous media: Coupling molecular dynamics simulations and theoretical model. Adv. Water Resour. 165, 104239. https://doi.org/10.1016/j.advwatres.2022.104239.
Wang, H., Cai, J., Su, Y., Jin, Z., Zhang, M., Wang, W., Li, G., 2023a. Pore-scale study on shale oil–CO2–water miscibility, competitive adsorption, and multiphase flow behaviors. Langmuir 39, 12226–12234. https://doi.org/10.1021/acs.langmuir.3c01570.
Wang, W., Xie, Q., An, S., Bakhshian, S., Kang, Q., Wang, H., Xu, X., Su, Y., Cai, J., Yuan, B., 2023b. Pore-scale simulation of multiphase flow and reactive transport processes involved in geologic carbon sequestration. Earth-Sci. Rev 247, 104602. https://doi.org/10.1016/j.earscirev.2023.104602.
Yang, Y., Wang, J., Wang, J., Li, Y., Sun, H., Zhang, L., Zhong, J., Zhang, K., Yao, J., 2023a. Pore-scale modeling of coupled CO2 flow and dissolution in 3D porous media for geological carbon storage. Water Resour. Res. 59, e2023WR035402. https://doi.org/10.1029/2023WR035402.
Yang, Y., Wang, J., Wang, J., Zhang, Q., Yao, J., 2023b. Pore-scale numerical simulation of supercritical CO2-brine two-phase flow based on VOF method. Nat. Gas Ind. B 10, 466–475. https://doi.org/10.1016/j.ngib.2023.08.002.
Yang, E., Baek, S., Kwon, T.-H., Yun, T.S., 2024. X-ray CT-based interpretation of microbial-induced carbonate precipitation and local hydraulic behaviors. Eng. Geol. 330, 107426. https://doi.org/10.1016/j.enggeo.2024.107426.
Yu, C., Jiang, Q., Pu, W., Su, N., 2022. Quantitative analysis of CO2 miscible flooding in tight formation at pore scale applying nuclear magnetic resonance. Pet. Sci. Technol. 40, 2038–2048. https://doi.org/10.1080/10916466.2022.2047064.
Yu, B., Dijkstra, T.A., Fan, W., Smalley, I.J., Wei, Y.N., Deng, L.S., 2024. Advanced multi-scale characterization of loess microstructure: Integrating μXCT and FIB-SEM for detailed fabric analysis and geotechnical implications. Eng. Geol. 341, 107727. https://doi.org/10.1016/j.enggeo.2024.107727.
Zhang, P., Lu, S., Li, J., Zhang, J., Xue, H., Chen, C., 2018. Permeability evaluation on oil-window shale based on hydraulic flow unit: a new approach. Adv. Geo-Energy Res. 2, 1–13. https://doi.org/10.26804/ager.2018.01.01.
Zhao, Z., Zhou, X.-P., 2023. A novel voxel-particle energy approach to predict 3D microscopic fracture surface of porous geomaterials and fracture permeability modeling. Eng. Geol. 323, 107214. https://doi.org/10.1016/j.enggeo.2023.107214.
Zhou, Y., Guan, W., Zhao, C., Zou, X., He, Z., Zhao, H., 2023. Spontaneous imbibition behavior in porous media with various hydraulic fracture propagations: a pore-scale perspective. Adv. Geo-Energy Res. 9, 185–197. https://doi.org/10.46690/ager.2023.09.06.
Zhu, Q., Wu, K., Guo, S., Peng, F., Zhang, S., Jiang, L., Li, J., Feng, D., Zhang, Y., Chen, Z., 2024. Pore-scale investigation of CO2-oil miscible flooding in tight reservoir. Appl. Energy 368, 123439. https://doi.org/10.1016/j.apenergy.2024.123439.